



Study on the Wear and Corrosion Resistance of CoCrFeNiTi_{0.8}-x_cBN Laser Cladding Coatings

Zhongsheng Li¹ · Kaiqiang Song¹ · Yixin Bai¹ · Dalong Cong¹ · Min Zhang¹ · Dong Peng¹ · Xuan Wang¹ · Xingxing Ding¹ · Miaomiao Liao² · Fu Zhou¹ · Zehui Hua¹ · Changpeng Wang¹

Submitted: 21 January 2024 / in revised form: 15 April 2024 / Accepted: 17 April 2024 / Published online: 23 May 2024
© ASM International 2024

Abstract This work aimed to explore the effect of cBN (cubic boron nitride) content on the microstructures and wear-corrosion resistance of the CoCrFeNiTi_{0.8}-x_cBN ($x = 0, 2, 4, 6$ wt.%) particle-reinforced high-entropy alloy coatings. Laser cladding technology was used to prepare the coatings on TC18 substrate. The microstructures, volume wear rates and polarization curves were characterized. The results showed that the CoCrFeNiTi_{0.8}-x_cBN coatings had an optimal forming quality under the process parameters: laser power of 1500 W, scanning rate of 12 mm/s and overlapping rate of 60%. As the cBN content increased, plenty of TiN and TiB₂ hard particles formed in situ in the coatings, significantly improved the wear resistance. As a result, the volume wear rate of CoCrFeNiTi_{0.8}-6_cBN was only 4.0% and 16.5% of that of TC18 substrate and CoCrFeNiTi_{0.8} coating, respectively; the wear mechanism changed from adhesive wear + oxidative wear to abrasive wear + oxidative wear gradually. Moreover, CoCrFeNiTi_{0.8}-x_cBN coatings can effectively inhibit the infiltration of corrosive media by dense organizational characteristics and the physical barrier effect of oxidation-protective films. After 480 h of neutral salt spray (NSS) test, the CoCrFeNiTi_{0.8}-x_cBN coatings exhibited excellent corrosion resistance, both of the appearance and protection rating reached level 10. Therefore, it can be used as the wear-corrosion-resistant coating for the TC18 substrate in a NSS environment.

Keywords CoCrFeNiTi_{0.8}-x_cBN · high entropy · laser cladding · microstructure · wear-corrosion-resistant

Introduction

TC18, a kind of $\alpha + \beta$ type structure titanium alloy, is widely used in aircraft landing gear and other heavy-load structural components by virtue of its high specific strength and excellent corrosion resistance (Ref 1, 2). However, low hardness leads the TC18 titanium alloy to fail under heavy-load service condition by excessive wear; therefore, it is urgent to carry out research on preparing wear-corrosion resistant coating on the surface of TC18 substrate (Ref 3, 4).

At present, the wear protection treatments for titanium alloys mainly include chromium plating, thermal spraying and laser cladding, etc. Compared to chromium plating and thermal spraying, laser cladding technology has the following advantages (Ref 5, 6). Firstly, the cladding coatings are well bonded to the substrate by metallurgical bonding; secondly, laser cladding has transient laser irradiation time and excessive subcooling, so it is easy to obtain the coatings with fine grains and exhibit excellent mechanical properties; thirdly, it is able to realize selective melting with high efficiency, which can effectively reduce the waste of the raw material.

As a new type of material developed in the field of metal materials in recent years, high-entropy alloys (HEAs) are composed of 5 to 13 different elements, with molar ratios of each element ranging from 5 to 35%. It is characterized by large lattice distortion and high configurational entropy (Ref 7, 8). HEAs are chemically stable and have excellent corrosion resistance based on the thermodynamically unique high-entropy effect that effectively inhibits the

✉ Yixin Bai
bitbyx@163.com

¹ Southwest Institute of Technology and Engineering, Chongqing 400039, China

² Chongqing Optoelectronics Research Institute, Chongqing 400060, China

Table 1 Chemical composition of TC18 substrate

Element	Al	Mo	V	Cr	Fe	Impurity	Ti
Content, wt.%	4.4-5.7	4.0-5.5	4.0-5.5	0.5-1.5	0.5-1.5	≤ 0.1	Rest

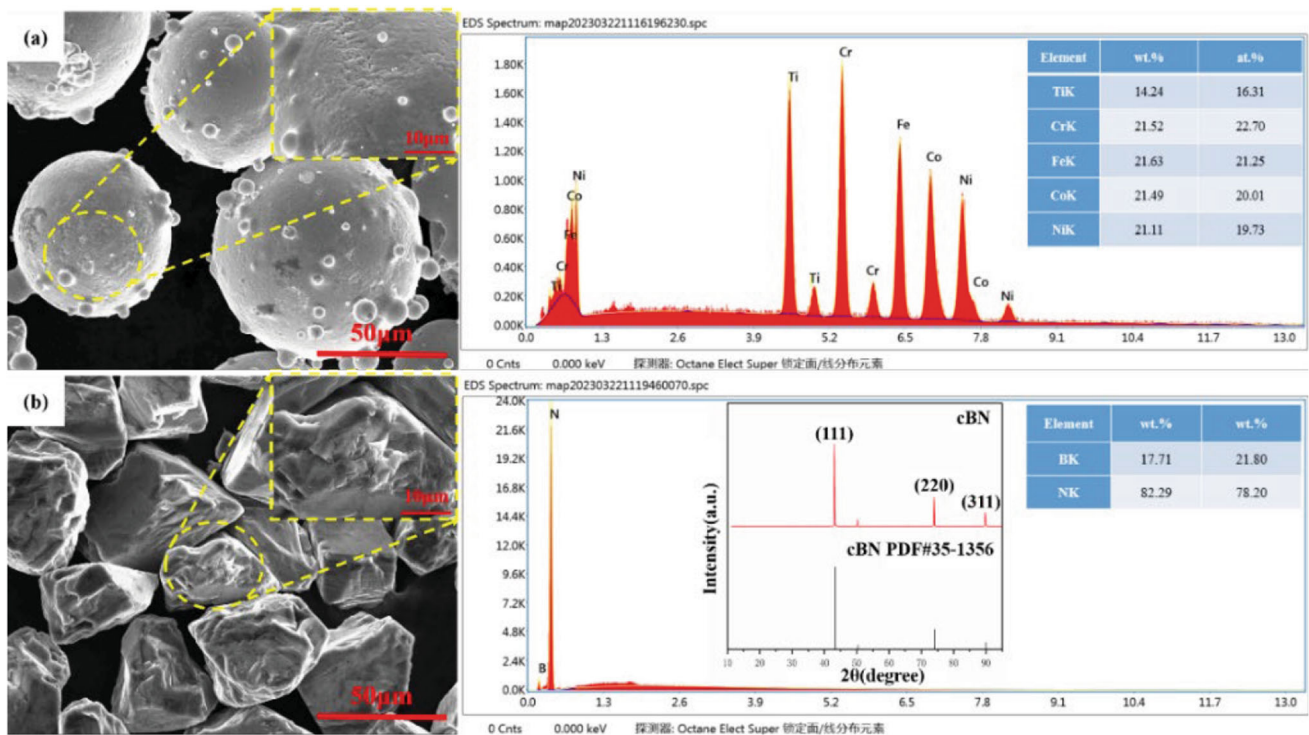


Fig. 1 SEM images and composition of laser cladding feedstock powders: (a) CoCrFeNiTi_{0.8}; (b) cBN

Table 2 A single-variable experiment of laser cladding

Cladding speed	Laser power		
	1200 W	1500 W	1800 W
10 mm/s	A1	A2	A3
12 mm/s	A4	A5	A6
14 mm/s	A7	A8	A9

Table 3 Main parameters of neutral salt spray (NSS) test

Parameter	Value
Salt solution concentration, wt.%	5.1
Chamber temperature, °C	35-36
Salt solution, pH	6.83-6.86
Sedimentation, mL/80 cm ³ h	1.70
Chamber pressure, kPa	96.53-124.11

formation of intermetallic compounds (Ref 9, 10). In addition, HEAs also exhibit hysteretic diffusion effect in dynamics (Ref 11), lattice distortion effect in structure (Ref 12) and “cocktail” effect in performance (Ref 13), which enable them to combine high strength and toughness with excellent wear resistance compared to other metal materials. Guo et al. (Ref 14) prepared in situ TiN particles reinforced CoCr₂FeNiTi_x ($x = 0, 0.5, 1$) HEAs coating on 904L stainless steel by laser cladding, the hardness of the coating was more than three times that of the substrate as

$x = 1$, and its abrasion loss was about 1/3 of that of the 904L stainless steel substrate.

Due to the similarity of atomic radius and electronegativity of Co, Cr, Fe and Ni elements, CoCrFeNi-based HEAs are prone to form a single FCC-type solid solution with excellent toughness and corrosion resistance (Ref 15). However, low hardness limits their application in heavy-load friction service conditions. Research shows that (Ref 16-18) the addition of Ti element can intensify the lattice distortion and contribute to the formation of high hardness BCC phase along with the grain refinement, thereby improving the wear resistance of CoCrFeNi-based HEAs. While excess BCC phase would reduce the toughness and

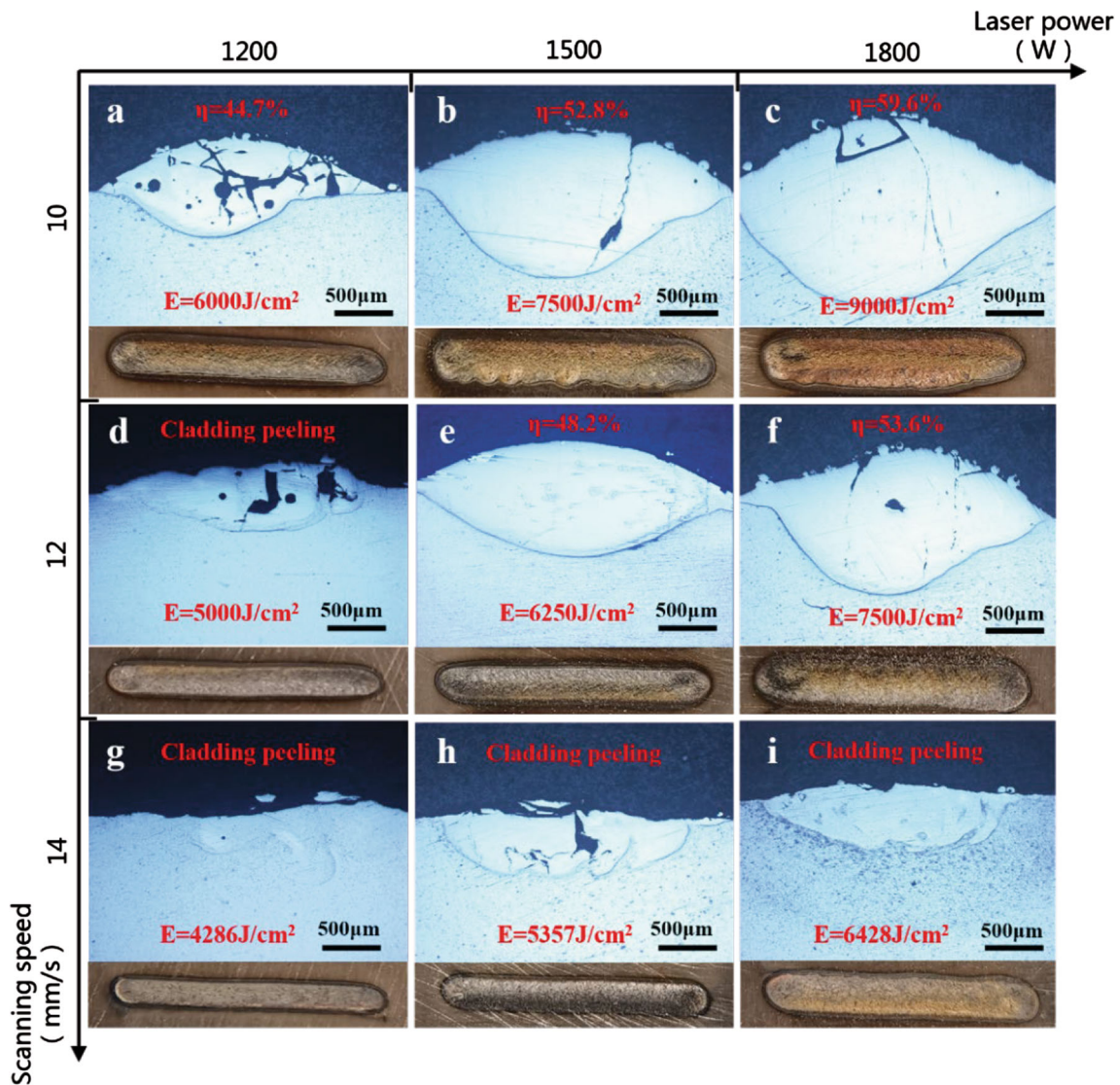


Fig. 2 Surface macro-morphology and cross-sectional metallography of CoCrFeNiTi_{0.8} cladding layer under different process parameters: (a) Test number A1; (b) Test number A2; (c) Test number A3;

(d) Test number A4; (e) Test number A5; (f) Test number A6; (g) Test number A7; (h) Test number A8; (i) Test number A9

ductility of CoCrFeNi-based HEAs, increase the sensitivity to cracking in the rapid cooling during the laser cladding process. Zuo found that (Ref 19) when the molar ratio of Ti element was 0.8 (CoCrFeNiTi_{0.8}), CoCrFeNiTi high-entropy alloy system reached the solubility limit, and the cladding coating exhibited the optimal comprehensive mechanical properties at this time, with a microhardness of 502.39 HV_{0.3}.

To further enhance the microhardness and wear resistance of CoCrFeNiTi_{0.8} coatings, cubic boron nitride (cBN) particles with ultra-high hardness (Ref 20) were selected as the reinforcing phase in this paper. A series of CoCrFeNiTi_{0.8}-xcBN ($x = 0, 2, 4, 6$ wt.%) composite coatings were prepared on the surface of TC18 substrate by

laser cladding technology. The effect of cBN content on the microstructures and wear-corrosion resistance property of the cladding coatings were studied.

Experimental

Experimental Raw Materials

TC18 titanium alloy was selected as the substrate for the laser cladding experiments; the nominal chemical composition is shown in Table 1. It was made into two specifications of 80 mm × 40 mm × 5 mm and 30 mm × 20 mm × 10 mm by EDM wire cutting for

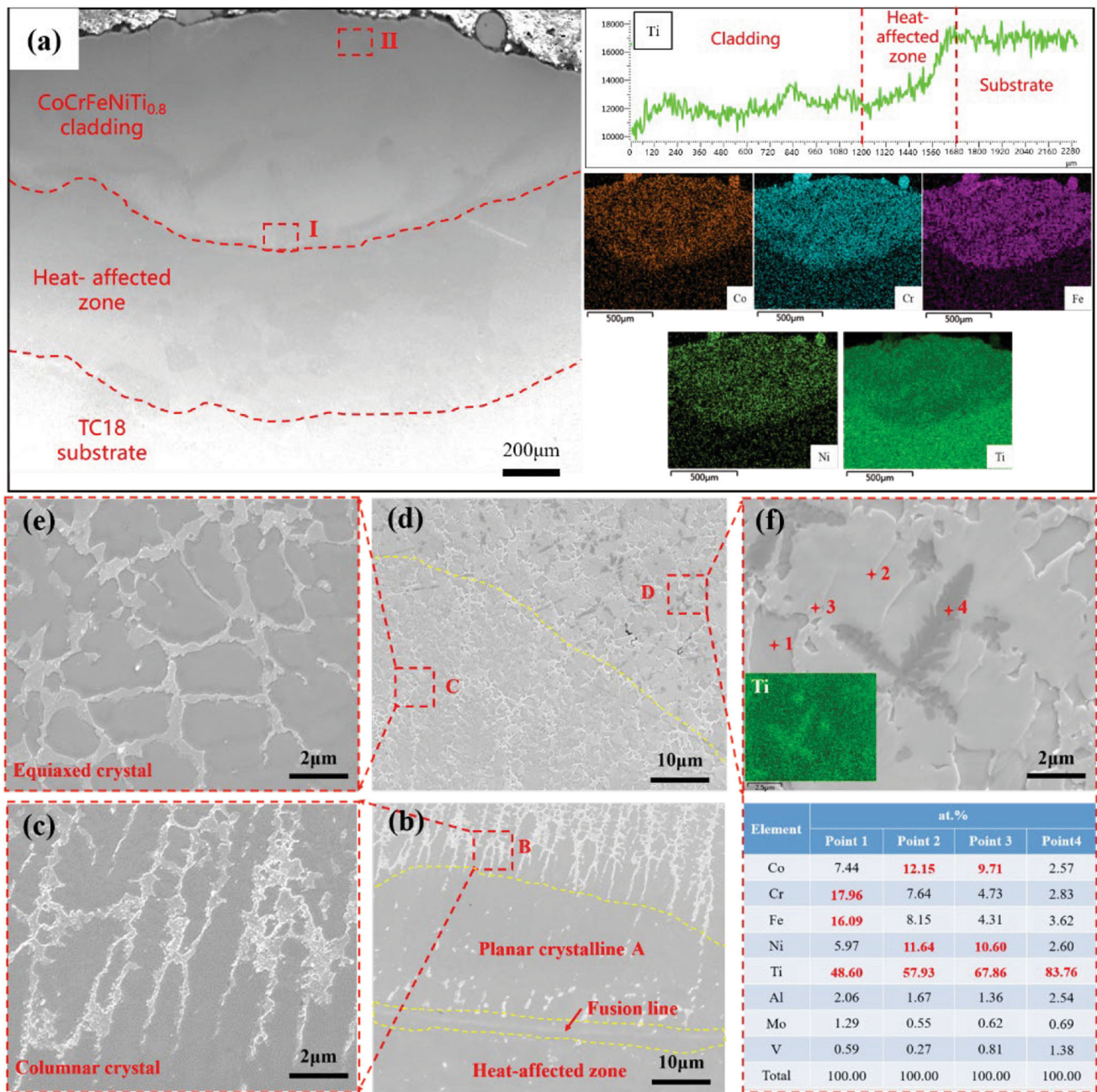


Fig. 3 Cross-sectional microstructures and composition distribution of CoCrFeNiTi_{0.8} cladding layer: (a) Overall cross-sectional microstructure and composition distribution (× 100); (b) Microstructure of region I (× 2000); (c) Microstructure of part A in region I

(× 10,000); (d) Microstructure of region II (× 2000); (e) Microstructure of part B in region II (× 10,000); (f) Microstructure and elemental composition of part C in region II (× 10,000)

cladding parameters optimization, friction-wear and neutral salt spray tests, respectively. The cladding powders used in this paper were mechanically mixed CoCrFeNiTi_{0.8}-xCBN ($x = 0, 2, 4, 6$ wt.%) which were numbered in order of C-0, C-2, C-4 and C-6. CoCrFeNiTi_{0.8} raw powder was supplied by Shanxi GUIZIDAN New Materials Co., Ltd., with the particle size of 50-150 μm (Fig. 1a); cBN raw powder was

supplied by Kaifeng Bescor Superabrasives Co., Ltd., with the particle size of 40-60 μm (Fig. 1b).

Preparation of the Coatings

The coatings involved in this experiment were prepared by LOM3000 laser cladding system (LATEC, China), equipped with MSFC-4000W laser (Chuangxin, China) and

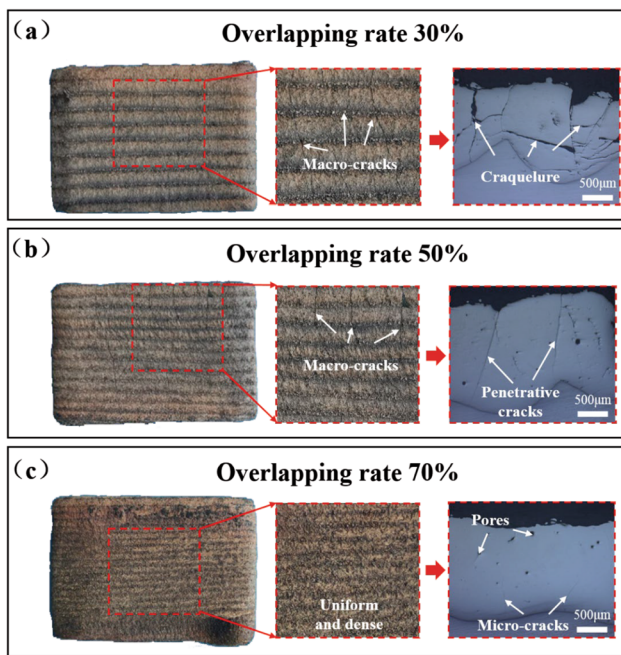


Fig. 4 Surface macro-morphology and cross-sectional metallography of CoCrFeNiTi_{0.8} cladding layer under different overlapping rates: (a) 20%; (b) 40%; (c) 60%

IRB2400 laser movement control system (ABB, Switzerland). The high-energy laser beam has a spot diameter of 2 mm. Before cladding, the TC18 substrate should be sanded with 180# sandpaper to remove the oil and oxide films on the substrate, and then preheated in a vacuum tube furnace at 200 °C for 2 h to moderate the thermal stress and reduce the cracking sensitivity of the coatings (Ref 21, 22).

During cladding process, Argon was selected as the powder feeding gas and protective gas; the laser defocusing distance was 20 mm, and the fixed powder feeding rate was 1.0 rpm. In order to investigate the optimal matching of laser power and cladding speed, a univariate experiment was designed as shown in Table 2, with laser powers of 1600W, 1800W and 2000W and scanning rates of 10 mm/s, 15 mm/s and 20 mm/s, respectively.

Friction-Wear Test

A reciprocating tribometer (HSR-2M, China) was used for carrying out the friction-wear test of the CoCrFeNiTi_{0.8}-xCBN cladding coatings under standard atmospheric conditions (20–25 °C and relative humidity 35–50%). The Al₂O₃ grinding balls with a diameter of 5 mm were selected as the friction counterparts. The tribological experimental conditions were set as follows: applied load of 20 N, sliding length of 3 mm, sliding frequency of 5 Hz and duration of 1800 s. Before the friction-wear test, the coating samples should be lathed, sanded by 600#, 1000#,

1500# sandpapers and polished by OPS polishing solution sequentially to ensure the surface roughness $R_a < 0.1 \mu\text{m}$. The surface roughness of TC18 substrate and CoCrFeNiTi_{0.8}-xCBN coating samples was measured by TR200 roughness meter (Xintian, China). The friction coefficients were recorded in real time during the test. The volume wear rates can be calculated by the equation $K = V/(P \times L)$ (Ref 23), where K is the wear rates ($\text{mm}^3/\text{N m}$), V is the wear volume loss (mm^3), P is the normal load applied (N) and L is the total sliding distance (m). The friction-wear tests for each sample were repeated three times, and the average of the three tests was taken for the volume wear rates.

Neutral Salt Spray Test

Neutral salt spray test (NSS) was carried out on CCX-2000 cyclic corrosion test chamber (ATLAS, USA) according to National military standard of GJB 150.11A-2009 (Ref 24). The coating samples were placed on a sample frame with a vertical line of 25°. The specific process parameters of the NSS test are shown in Table 3. After spraying 24 h continuously, the samples were dried for 24 h under standard atmospheric conditions (23.0–23.5 °C and relative humidity 49–50%) as a cycle. The NSS test was totally conducted for ten cycles (480 h).

Characterization

The microstructures and component distribution of the cladding powders and coatings were observed by scanning electron microscopy (SEM, Hitachi S4800, Japan) on an instrument equipped with energy-dispersive spectroscopy (EDS; Oxford EI350, UK). The porosity of CoCrFeNiTi_{0.8}-xCBN coatings was determined according to the standard of ISO/TR 26946-2011 (Ref 25) and calculated by the software Image pro plus. The phase compositions of the coatings were characterized by X-ray diffraction (XRD, Smartlab-9, Japan). The microhardness was measured by the standard Vickers hardness tester (HM-MT 1000, China) under 500 g. The wear scar sizes of TC18 substrate and CoCrFeNiTi_{0.8}-xCBN coatings were characterized by LEXT-OLS4000 laser scanning confocal microscope (OLYMPUS, Japan). The polarization curves of the samples before and after NSS test were measured three times by P4000A electrochemical workstation (Princeton, USA) at a scan rate of 0.5 mV/s from -0.8 to 0.6 V/SCE; for each measurement, the test area of coating samples was $10 \times 10 \text{ mm}^2$; platinum and saturated calomel electrode (SCE) were used as the counter electrode and the reference electrode, respectively.

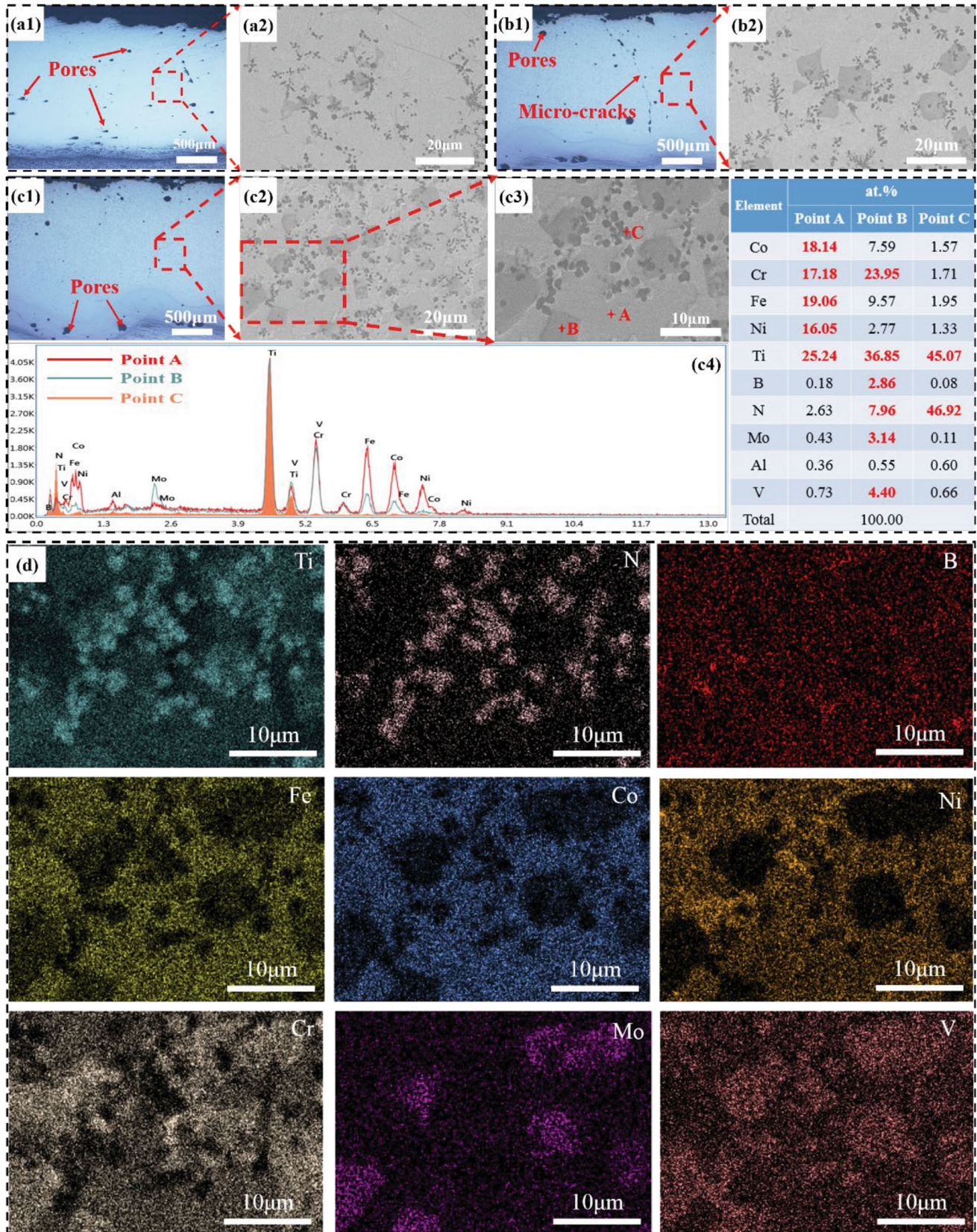


Fig. 5 Cross-sectional microstructures and composition distribution of CoCrFeNiTi_{0.8-x}CBN cladding layers: (a1) Microstructures of C-2 ($\times 100$); (a2) Microstructures of C-2 ($\times 2500$); (b1) Microstructures of C-4 ($\times 100$); (b2) Microstructures of C-4 ($\times 2500$); (c1) Microstructures of C-6 ($\times 100$); (c2) Microstructures of C-6 ($\times 2500$); (c3) Microstructures of C-6 ($\times 5000$); (c4) Point scan results of C-6; (d) Mapping results of C-6 ($\times 2500$).

Results and Discussion

Microstructures and Component Distribution of the CoCrFeNiTi_{0.8} Coatings

The surface macrographs and cross-sectional metallographic structures of single-pass CoCrFeNiTi_{0.8} cladding coatings (C-0) under different cladding parameters are displayed in Fig. 2. As it is shown in illustration, the dilution rate η (shown in Eq 1) of the coatings increased significantly as the increase of laser power when the scanning rate is constant. Also, the dilution rate η decreased with the increase of scanning rate when the laser power is constant. This phenomenon was due to a positive correlation between the dilution rate η and laser energy density E (shown in Eq 2).

$$\eta = h/(H + h) \quad (\text{Eq 1})$$

where η is the dilution rate of the cladding coatings (%), H is the distance between the top of cladding coating and the substrate plane (m), and h is the distance between the bottom of the molten pool and the substrate plane (m).

$$E = P/(DV) \quad (\text{Eq 2})$$

where E is the laser energy density (J/cm^2), P is the laser power (W), D is the diameter of the laser beam (mm), and V is the laser scanning rate (mm/s).

When the laser power was 1200 W, there were a large number of penetrating cracks in the A1 sample (Fig. 2a), and the dilution rate was only 44.7%. Indicating that the CoCrFeNiTi_{0.8} cladding powder cannot melt fully at this power, the accumulation of unmelted particles led to an increasing defect inside the coating. As the laser scanning rate further increased, the laser energy density E dropped significantly, resulting in incomplete formation of A4 (Fig. 2d) and A7 (Fig. 2g) claddings coatings.

As the laser power increased to 1500 W, the crack sensitivity inside the cladding coatings decreased obviously. The dilution rate of A2 (Fig. 2b) was increased to 52.8%, with only a few microcracks formed due to thermal stress concentration during rapid cooling. When the scanning rate was increased to 12 mm/s, the corresponding laser energy density was $6250 \text{ J}/\text{cm}^2$, the A5 coating sample (Fig. 2e) exhibited an ideal cladding state without penetrating cracks and pores and the dilution rate was

48.2% in this condition. As the scanning rate was further increased to 14 mm/s, the laser energy density acting on A8 (Fig. 2h) dropped to $5357 \text{ J}/\text{cm}^2$ and caused the decline in cladding quality; plenty of defects appeared, and coating spalling occurred.

When the laser power reached 1800 W, the dilution rate of the A3 (Fig. 2c) with a scanning rate of 10 mm/s reached 59.6%. High dilution led to excessive introduction of elements inside the TC18 substrate and reduced the microhardness of cladding coatings. Meanwhile, the disturbance effect of laser beam on molten pool became greater under high laser energy density (Ref 26); as a result, more splashing particles appeared around the CoCrFeNiTi_{0.8} cladding coating and led to a decline in cladding quality. As the scanning rate increased, the cladding quality of A6 and A9 improved obviously, while there were still a few microcracks inside the coating. In summary, the laser power of 1500 W and the scanning rate of 12 mm/s were selected as the proper laser cladding parameters.

Figure 3 shows the cross-sectional microstructures and component distribution of single-pass C-0 coating under optimal parameters. As it is shown in Fig. 3(a), the cross-section of C-0 was divided into three zones: cladding zone with a thickness of 1200 μm , heat-affected zone with a thickness of 450 μm and TC18 substrate zone. Combined with EDS results, it can be found that all the elements of Co, Cr, Fe, Ni and Ti distributed uniformly in the cladding zone. The content of Ti exhibited a gradient transition from cladding zone (low Ti concentration) to TC18 substrate zone (high Ti concentration), indicating that a dense metallurgical bonding formed between the cladding coating and TC18 substrate.

According to the high-magnification SEM images shown in Fig. 3(b) and (c), the region I at the interface between the cladding layer and the heat-affected zone was mainly composed of planar crystal A and columnar crystal B; obvious fusion lines can be found as well. According to the theory of rapid solidification (Ref 27), TC18 substrate had the largest temperature gradient G and cladding coating had the lowest solidification rate R at the early stage of solidification. Therefore, the CoCrFeNiTi_{0.8} cladding coating crystallized epitaxial from the substrate in the form of non-uniform nucleation, resulting in a formation of fine planar crystals with a thickness of 15 μm . As the distance from the TC18 substrate increased, the temperature gradient G decreased and the solidification rate R increased gradually, causing a significant increase in concentrate gradient, thus a large number of columnar crystals grow upon the fine planar crystals.

As for the top of the molten pool, huge temperature gradient formed by air convection led to significant increase in solidification rate R . Plenty of fine equiaxial

crystals C appeared in region II (Fig. 3d, e). Besides that, a region D mainly containing dendritic crystals can be found at the top of the coating (Fig. 3f). By characterizing the composition of the top of CoCrFeNiTi_{0.8} coating (Fig. 3f), it can be found that the dark-gray structure 1 was the high melting point phase rich in Cr-Fe-Ti which took the lead in crystallization during solidification; the light-gray structure 2 was the low melting point phase rich in Co-Ni-Ti which precipitated attached to the high melting point phase; the bright-white structure 3 was (Ni, Co)Ti₂ Laves phase formed by precipitation of the supersaturated Ti in the low melting point phase; and the black structure 4 was the β-Ti phase precipitated non-equilibrium on the surface of molten pool under extreme undercooling.

The surface macrographs and cross-sectional metallographic structures of multi-pass C-0 coatings under different overlapping rates are shown in Fig. 4. It can be found that multi-pass C-0 coatings were poor flatness under the overlapping rates of 20% and 40%, plenty of

penetrative cracks perpendicular to the cladding direction appeared inside the coating. When the overlapping rate was increased to 60%, the surface flatness of C-0 improved significantly and cracks disappeared, exhibited uniform and dense cross-sectional microstructures. Qiao (Ref 28) found that the cracks formed in the multi-pass coatings were non-genetic defects. There was an obvious stress mutation at the lap under low overlapping rate, which was easy to induce the initiation and propagation of cracks. As the overlapping rate increased, the high-energy laser beam preheated the TC18 substrate more adequate, thereby reduced the temperature gradient between molten pool and the substrate and relieved the thermal stress, the cracking sensitivity of cladding coating was significantly reduced (Ref 6, 29).

As a result, the subsequent coating samples of CoCrFeNiTi_{0.8}-2cBN (C-2), CoCrFeNiTi_{0.8}-4cBN (C-4) and CoCrFeNiTi_{0.8}-6cBN (C-6) were prepared by the overlapping rate of 60%.

Table 4 Mixing enthalpy of different atom pairs [30]

Mixing enthalpy, kJ/mol	Co	Cr	Fe	Ni	Ti	B	N	V	Mo
Co	...	- 4	- 1	0	- 28	- 24	- 75	- 7	- 5
Cr	- 1	- 7	- 7	- 31	- 107	- 2	0
Fe	- 2	- 17	- 26	- 87	- 7	- 2
Ni	- 35	- 24	- 69	- 18	- 7
Ti	- 58	- 190	- 2	- 4
B	- 28	- 42	- 34
N	- 143	- 115
V	0
Mo

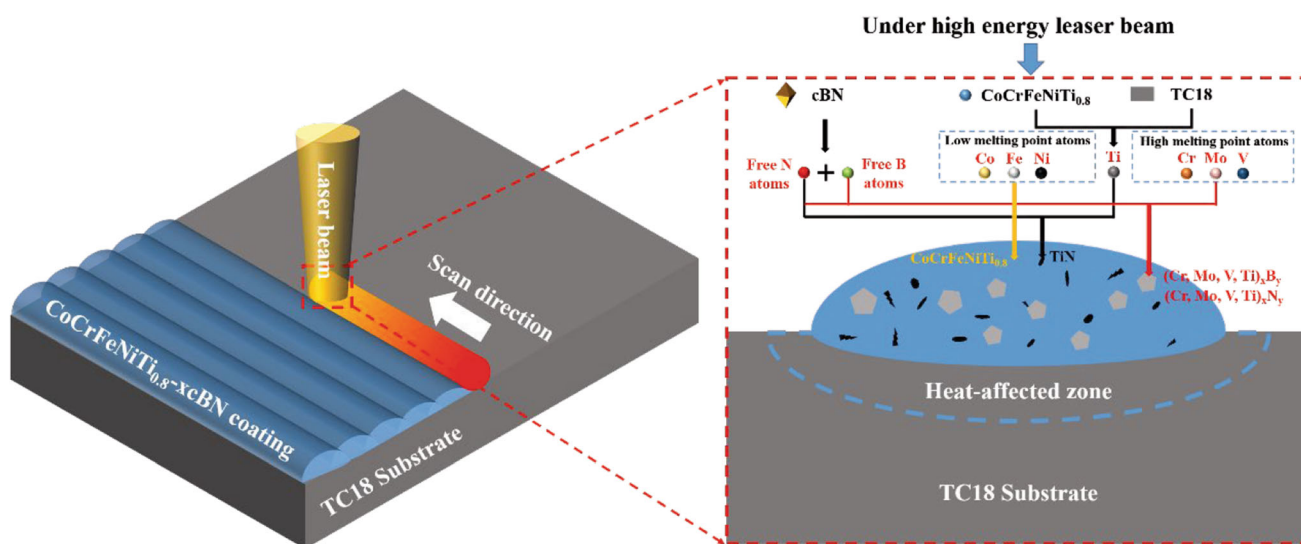


Fig. 6 Schematic diagram of microstructures formation mechanism of the CoCrFeNiTi_{0.8}-xcBN coatings during laser cladding process

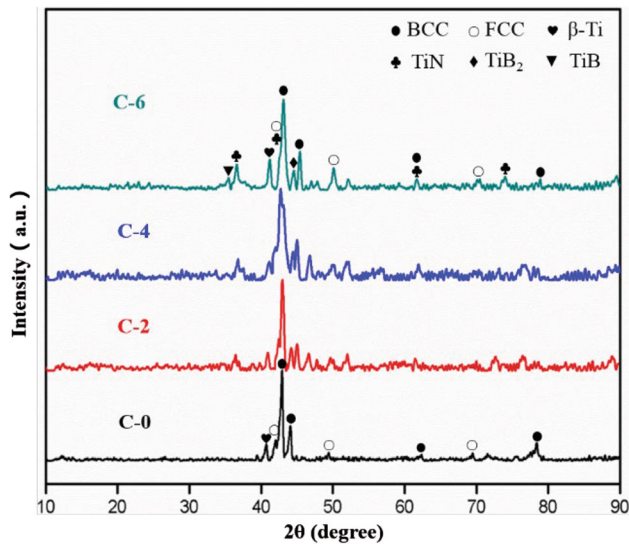


Fig. 7 XRD patterns of the CoCrFeNiTi_{0.8}-xcBN cladding layers

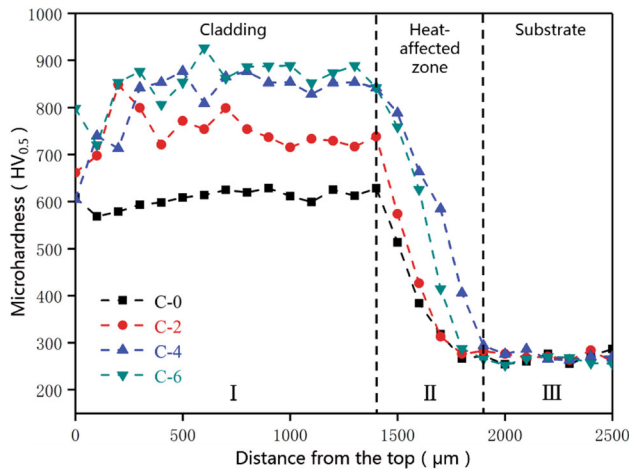


Fig. 8 Microhardness of the CoCrFeNiTi_{0.8}-xcBN cladding layers

Figure 5 shows the cross-sectional microstructures and component distribution of multi-pass C-2, C-4 and C-6 coatings. As it is shown in Fig. 5(a1), (b1) and (c1), all of the CoCrFeNiTi_{0.8}-xcBN coatings were metallurgical bonded to the TC18 substrate, only a small number of pores and microcracks dispersed inside the coatings, with a porosity less than 1%. According to the high-magnification SEM images shown in Fig. 5(a2), (b2), (c2) and (c3), all of the C-2, C-4 and C-6 coatings were composed of large-area light-gray structure A, unmelted-granular dark-gray structure B and dispersed black structure C. As the cBN content increased, the content of B and C increased accordingly, and the distribution uniformity was also significantly improved.

Combined with the EDS results (Fig. 5c4, d), the light-gray structure A mainly consisted of Co, Cr, Fe, Ni and Ti elements with an atomic ratio closed to that of C-0 coating,

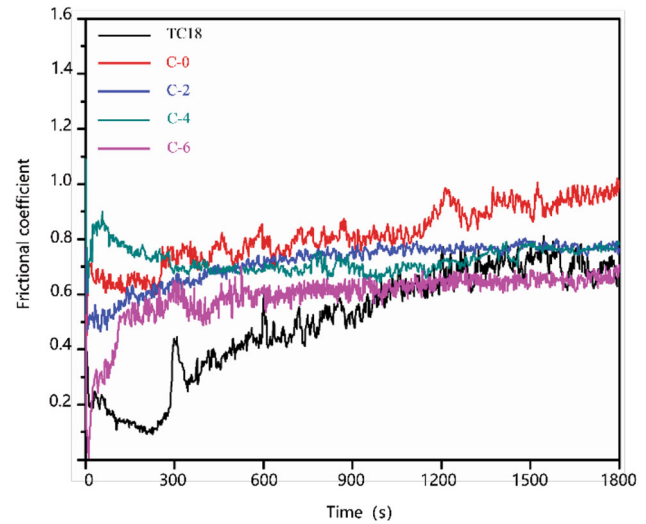


Fig. 9 Friction coefficient of the CoCrFeNiTi_{0.8}-xcBN cladding layers

indicating that A was the original CoCrFeNiTi_{0.8} coating structure. For the dark-gray structure B, there was an obvious accumulation of high melting point elements of Cr, Mo and V. Meanwhile, structure B presented a morphology of unmelted particles. It can be speculated that structure B was the refractory compounds ((Cr, Mo, V, Ti)_xB_y, (Cr, Mo, V, Ti)_xN_y) which formed by the high melting point elements reacted with free B and N atoms in the molten pool. The black structure C was mainly composed of Ti and N, with an atomic ratio close to 1:1. According to the mixing enthalpy of different atom pairs shown in Table 4 (Ref 30), the atoms between Ti and N had extremely low mixing enthalpy of -190 kJ, free N atoms preferentially combined with the excess Ti atoms and generated TiN phase in situ. With the increase of cBN content, freer B and N atoms appeared in the molten pool and the TiN gradually transformed from aggregated herringbone crystals to dispersed granular crystals, further enhanced the effect of dispersion strengthening.

In summary, a schematic diagram of microstructures evolution mechanism of the CoCrFeNiTi_{0.8}-xcBN coatings during laser cladding process is displayed in Fig. 6. It can be found that a molten pool contained free B, N, Co, Fe, Ni, Cr, Mo, V and Ti atoms formed under the high-energy laser beam; all the atoms were well-distributed and rearranged in the molten pool. During the cooling process, part of high melting point atoms (Cr, Mo, V) combined with free N, B and Ti atoms and took the lead in precipitating refractory compounds of (Cr, Mo, V, Ti)_xB_y and (Cr, Mo, V, Ti)_xN_y. And then, a large amount of Ti atoms provided by TC18 substrate combined with N atoms generated uniformly distributed TiN phase. Finally, low melting point atoms (Co, Fe, Ni, Ti) solidified to the initial

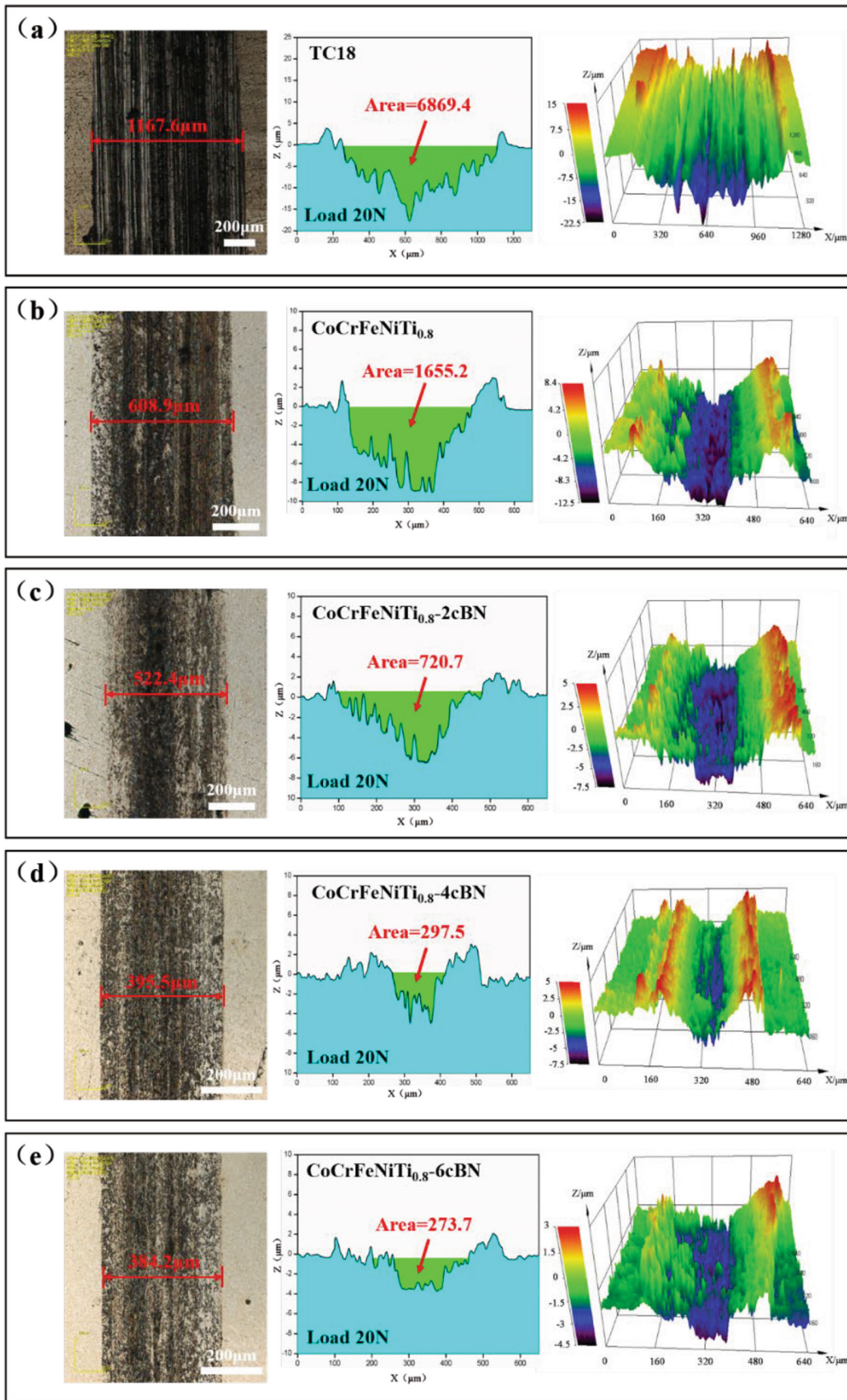


Fig. 10 2D/3D morphologies of the wear scars for CoCrFeNiTi_{0.8}-xcBN cladding layers: (a) TC18; (b) C-0; (c) C-2; (d) C-4; (e) C-6

microstructures of the CoCrFeNiTi_{0.8} coatings such as Co-Ni-Ti, (Ni, Co)Ti₂ Laves phase and β -Ti.

Phase Composition of the CoCrFeNiTi_{0.8}-xcBN Coatings

The phase composition of C-0, C-2, C-4 and C-6 coatings are shown in Fig. 7. It can be found that C-0 was mainly composed of face-centered cubic phase (FCC), body-centered cubic phase (BCC) and β -Ti; the diffraction peak of Laves phase cannot be found because of its low content. With the addition of cBN, there were no obvious cBN diffraction peaks in the C-2, C-4 and C-6. Instead, high melting point phases such as TiN, TiB, TiB₂ and Cr₂N appeared in the XRD pattern and the intensity of the diffraction peaks enhanced gradually as the cBN content increased. This phenomenon indicated that cBN was fully melted under the high-energy laser beam. The B and N atoms existed in a free state in the molten pool and combined with cations with lower mixing enthalpy to form compounds and precipitate preferentially. However, due to the high mixing enthalpy of B and N atoms, reaching -28 kJ/mol (Table 4), the priority of combining to each other was relatively low. Therefore, there was no obvious cBN diffraction peak in the XRD pattern.

Friction-Wear Property of the CoCrFeNiTi_{0.8}-xcBN Coatings

Figure 8 shows the cross-sectional microhardness curves of C-0, C-2, C-4 and C-6. As it is shown in illustration, the microhardness from the top of the coating to TC18 substrate of the four samples remained similar trend, and the microhardness values fluctuated steadily inside the coatings. In the heat-affected zone, the microhardness of the four samples gradually decreased with the compositional gradient to a level of the TC18 substrate (266.6HV_{0.5}). In addition, combined with the findings above, the addition of cBN promoted the in situ precipitation of hard particles such as TiN and TiB₂ which distributed dispersedly in crystals. Moreover, free B and N atoms were dissolved in the BCC and FCC phases, further reducing the plastic deformation of the solid solution. As a result, the microhardness of the CoCrFeNiTi_{0.8}-xcBN coatings increased gradually as the addition of cBN increased under the dual effects of diffusion strengthening and solid solution strengthening. The average microhardness of C-0, C-2,

C-4, and C-6 coating samples were 613.9HV_{0.5}, 755.1HV_{0.5}, 829.7HV_{0.5}, and 854.4HV_{0.5}, respectively.

The friction coefficient curves of the TC18 substrate and C-0, C-2, C-4, C-6 cladding coatings are shown in Fig. 9. It can be found that the friction coefficient of TC18 substrate was much lower than that of C-0, C-2, C-4 and C-6 samples in the early stage of friction-wear test, while it was opposite to the surface roughness, the surface roughness of TC18, C-0, C-2, C-4 and C-6 samples was Ra 0.05 μ m, Ra 0.07 μ m, Ra 0.08 μ m, Ra 0.09 μ m and Ra 0.09 μ m, respectively. Indicating that lower roughness brought less resistance and TC18 substrate exhibited lower friction coefficient in the initial state. However, along with the friction-wear test, the friction coefficients of TC18 and C-0 samples showed an increasing trend, and the growth rate of TC18 was higher than that of C-0 significantly. After 1800 s friction-wear test, the friction coefficient of TC18 was 0.65, and the friction coefficient of C-0 reached 0.96. C-2, C-4 and C-6 cladding coatings exhibited similar trend in friction coefficient which reached the maximum value at about 20 s and then fell back to a constant value between 0.6 and 0.7.

Figure 10 shows the 2D/3D morphologies of the wear scars on the TC18 substrate and C-0, C-2, C-4 and C-6 cladding coatings, respectively. It can be observed that the wear scar widths, wear scar cross-sectional areas and volume wear rates of all the five samples after the friction-wear test decreased accordingly with the improvement of the microhardness. The wear scar widths of TC18, C-0, C-2, C-4 and C-6 were 1167.6 μ m, 608.9 μ m, 522.4 μ m, 395.5 μ m and 384.2 μ m, respectively; the cross-sectional areas of wear scars were 6869.4 μ m², 1655.2 μ m², 720.7 μ m², 297.5 μ m² and 273.7 μ m²; corresponding volume wear rates are shown in Table 5, where the values of C-0, C-2, C-4 and C-6 are 24.1%, 10.5%, 4.3% and 4.0% of that of TC18 substrate, indicating that the preparation of the CoCrFeNiTi_{0.8}-xcBN coatings significantly enhanced the wear resistance property of the TC18 substrate.

Figure 11 shows the microstructures and oxygen element distribution of the wear scars on the TC18 substrate and C-0, C-2, C-4, and C-6 cladding coatings, respectively. As it is shown in Fig. 11(a), TC18 substrate occurred obvious plastic deformation under the cyclic load applied by the Al₂O₃ grinding ball due to its low microhardness and adhesion points formed on the friction surface. As the reciprocation of sliding friction, defects such as deep furrows and pits formed by peeling off the adhesion points appeared at the wear scars, and serious oxidation occurred at the wear scars as well. The wear mechanism of TC18 substrate was mainly manifested as adhesive wear and oxidative wear.

The wear scar depth of C-0 reduced significantly due to its microhardness is 2.3 times than that of TC18 substrate.

Moreover, C-0 coating exhibited a characteristic of abrasive wear with more wear debris. As the microhardness of C-0 coating was still much lower than that of the grinding ball, there were also a small number of pits formed by the peeling of adhesive points at the wear scar. Therefore, C-0 coating was manifested as a composite wear mechanism of abrasive wear, adhesive wear and oxidative wear. As a result of continuous peeling of adhesive points, the friction coefficient of TC18 substrate and C-0 coating gradually increased with the increase time of friction-wear test and led to higher volume wear rates.

As for the C-2, C-4, and C-6 coatings with higher microhardness (Fig. 11c-e), obvious oxidation also occurred at the wear scars, while the depth of wear scars was shallower and there were basically no defects such as furrows and pits. The wear mechanism was mainly manifested by abrasive wear and oxidative wear, where debris can form a protective substrate on the wear scars under the external loading and weaken the further wear by the grinding ball on the coating samples (Ref 31). Therefore,

the friction coefficient of C-2, C-4 and C-6 cladding coatings remained stable and exhibited lower volume wear rates and better wear resistance property.

Corrosion Resistance of the CoCrFeNiTi_{0.8}-x_cBN Coatings

The surface macrographs and potential polarization curves of the TC18 substrate and C-0, C-2, C-4 and C-6 cladding coatings before and after NSS test are shown in Fig. 12. Specific relevant electrochemical parameters obtained by Tafel extrapolation method are shown in Table 6. It can be found that there was no significant difference in the corrosion potential (E_{corr}) and corrosion current density (i_{corr}) of CoCrFeNiTi_{0.8}-x_cBN coatings before the NSS test. Due to the lower corrosion current density (i_{corr}) led to a lower corrosion rate (Ref 32), all the coating samples exhibited excellent corrosion resistance with the i_{corr} reached only the order of 10^{-7} , which was closed to that of the TC18 substrate ($i_{corr} = (5.2 \pm 0.3) \times 10^{-8}$).

Table 5 Volume wear rates of the CoCrFeNiTi_{0.8}-x_cBN cladding layers

Samples	Volume wear rate, mm ³ /N m	Loading, N	Total reciprocating sliding distance, m
TC18	$(2.3 \pm 0.1) \times 10^{-5}$	20	45
C-0	$(5.5 \pm 0.3) \times 10^{-6}$		
C-2	$(2.4 \pm 0.1) \times 10^{-6}$		
C-4	$(9.9 \pm 0.2) \times 10^{-7}$		
C-6	$(9.1 \pm 0.1) \times 10^{-7}$		

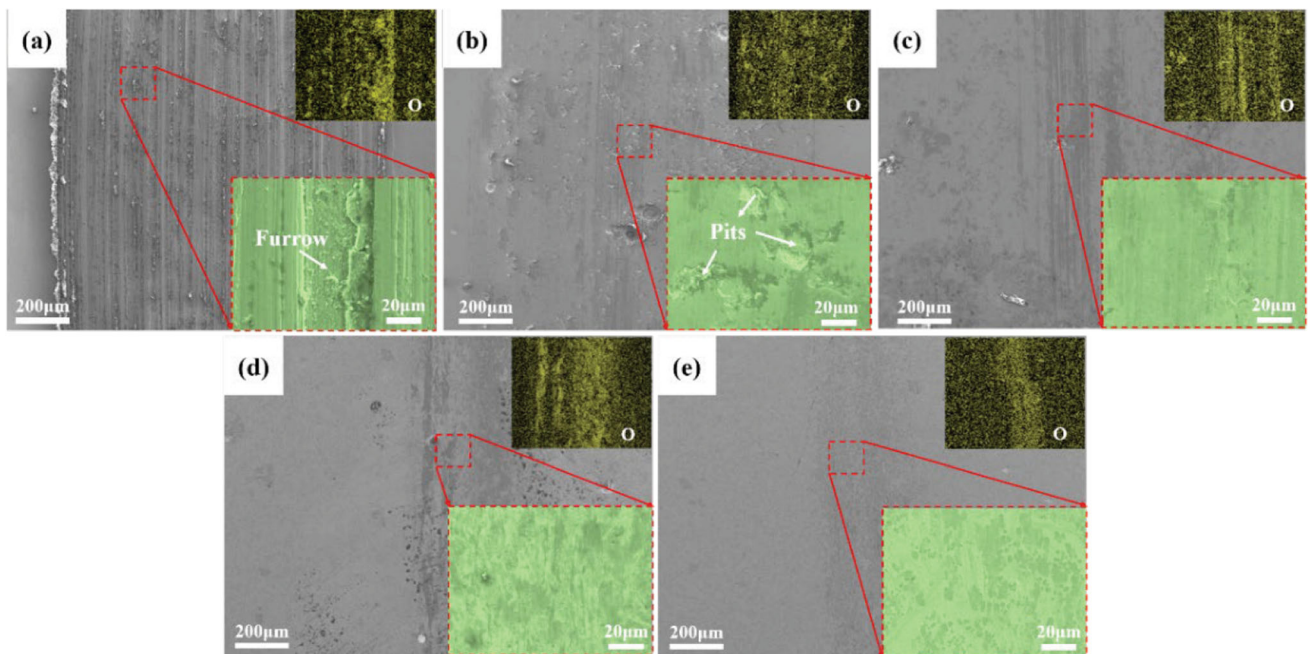


Fig. 11 Microstructures of the wear scars for CoCrFeNiTi_{0.8}-x_cBN cladding layers: (a) TC18; (b) C-0; (c) C-2; (d) C-4; (e) C-6

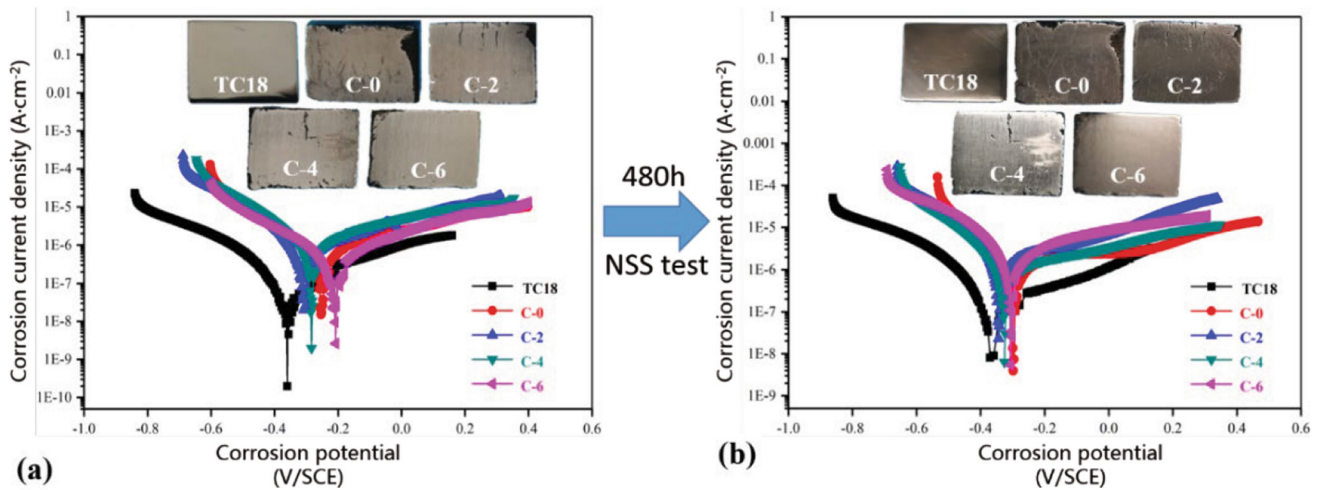


Fig. 12 The potentiodynamic polarization curves of CoCrFeNiTi_{0.8}-xcBN cladding layers before and after NSS test: (a) Before NSS test; (b) After 480 h NSS test

Table 6 Corrosion potential E_{corr} and current density i_{corr} of the samples before and after NSS test

Experimental condition	Samples	E_{corr} , V	i_{corr} , A cm ⁻²
Before NSS test	TC18	-0.36 ± 0.02	$(5.2 \pm 0.3) \times 10^{-8}$
	C-0	-0.25 ± 0.06	$(5.6 \pm 0.1) \times 10^{-7}$
	C-2	-0.30 ± 0.04	$(7.0 \pm 0.3) \times 10^{-7}$
	C-4	-0.28 ± 0.04	$(9.0 \pm 0.6) \times 10^{-7}$
	C-6	-0.29 ± 0.02	$(3.2 \pm 0.3) \times 10^{-7}$
After NSS test (480 h)	TC18	-0.37 ± 0.11	$(1.2 \pm 0.2) \times 10^{-7}$
	C-0	-0.30 ± 0.05	$(1.6 \pm 0.2) \times 10^{-6}$
	C-2	-0.34 ± 0.04	$(1.9 \pm 0.2) \times 10^{-6}$
	C-4	-0.33 ± 0.04	$(1.1 \pm 0.3) \times 10^{-6}$
	C-6	-0.31 ± 0.02	$(2.5 \pm 0.2) \times 10^{-6}$

After 480 h NSS test, the TC18 substrate and C-0, C-2, C-4 and C-6 coating samples still maintained great corrosion resistance, the i_{corr} of the coatings raised slightly to the order of 10^{-6} because a little corrosive medium remained in the defects of the samples and reduced their electric resistance (Ref 33, 34). There was no visible corrosion on the surface of all the samples, both of the appearance rating and protection rating reached 10 degrees (Ref 35), according to the cross-sectional microstructures and composition of C-6 shown in Fig. 13, there was also no obvious corrosive pitting inside the coating, the composition was well-distributed and the microstructures was consistent with that before the NSS test (Fig. 5c2, c3).

The excellent corrosion resistance of CoCrFeNiTi_{0.8}-xcBN is mainly attributed to the following reasons. Firstly, CoCrFeNiTi_{0.8}-xcBN coatings had an extremely dense microstructure, they can effectively inhibit the infiltration of corrosive medium such as Cl⁻ and H₂O; secondly, the corrosion resistant elements of Co, Cr, Ni and Ti played an important role in forming dense oxidation-protective films

such as Cr₂O₃ and TiO₂, which can prevent the further infiltration of corrosive medium and decelerate the development of the corrosion process; finally, similar corrosion potential (E_{corr}) between the CoCrFeNiTi_{0.8}-xcBN coatings and TC18 substrate provided little corrosion driving force, and the galvanic corrosion tendency at the interface of the coatings and substrate was low. As a result, the CoCrFeNiTi_{0.8}-xcBN cladding coatings can be used as a wear-resisting protective coating for TC18 substrate under the neutral salt spray environment. Moreover, combining the economy and comprehensive performance, CoCrFeNiTi_{0.8}-4cBN coating was optimal for further application.

Conclusions

- (1) The proper laser cladding parameters of CoCrFeNiTi_{0.8}-xcBN coatings were: laser power of 1500 W, scanning rate of 12 mm/s and overlapping

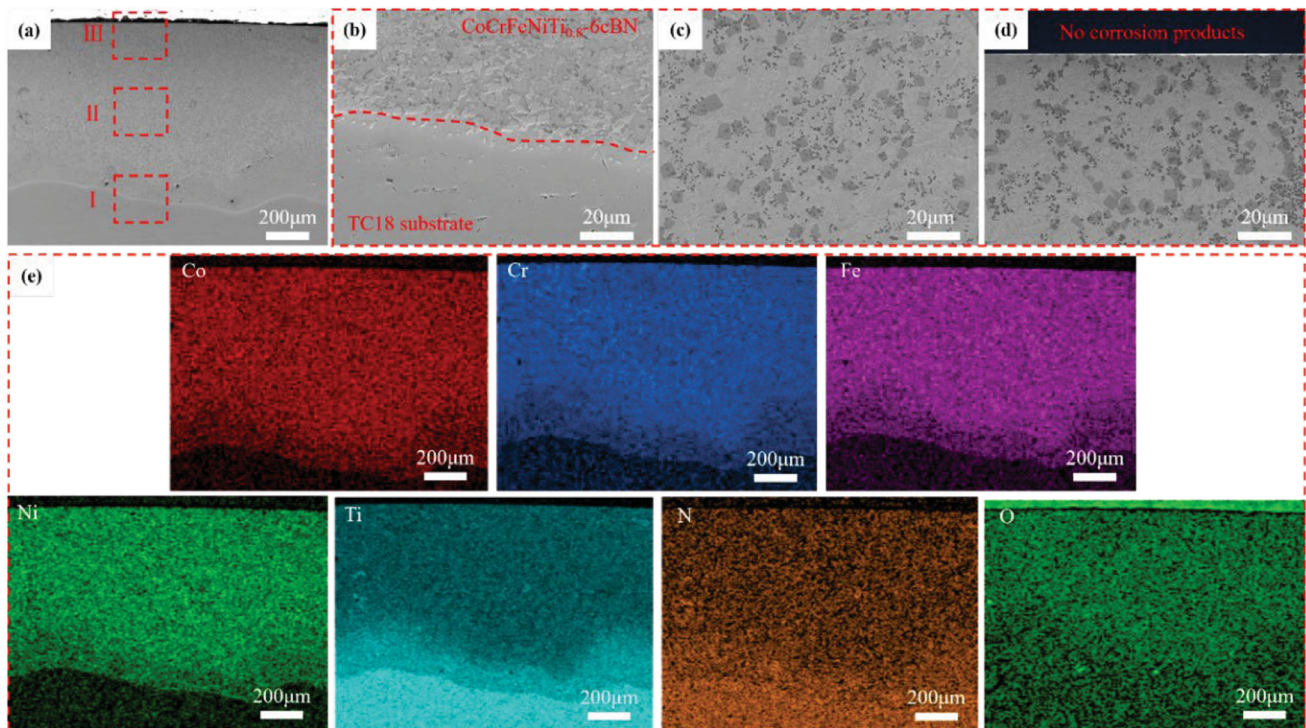


Fig. 13 Cross-sectional SEM images and composition of CoCrFeNiTi_{0.8}-6cBN coating after 480 h NSS test: (a) Low-magnification SEM images ($\times 100$); (b) High-magnification SEM images of region I ($\times 1000$); (c) High-magnification SEM images of region II

($\times 1000$); (d) High-magnification SEM images of region III ($\times 1000$); (e) Composition distribution of the CoCrFeNiTi_{0.8}-6cBN coating ($\times 100$)

rate of 60%; under the process, CoCrFeNiTi_{0.8}-xcBN had the best forming quality with dense microstructures and a moderate dilution rate of 48.2%.

- (2) With the addition of cBN, a large number of reinforced particles such as TiN and TiB₂ were formed in situ in the cladding coatings, significantly improving the microhardness and wear resistance of the CoCrFeNiTi_{0.8} coating. The volume wear rates of C-0, C-2, C-4 and C-6 were only 24.1%, 10.5%, 4.3%, and 4.0% of that of the TC18 substrate, respectively; and the wear mechanism gradually transformed from adhesive wear + oxidative wear to abrasive wear + oxidative wear.
- (3) Under the combined effect of dense microstructure and a physical barrier provided by oxidation-protective films, the CoCrFeNiTi_{0.8}-xcBN cladding coatings can effectively inhibited the further infiltration of corrosive medium of Cl⁻ and H₂O and slowed down the corrosion process. After 480 h NSS test, the CoCrFeNiTi_{0.8}-xcBN cladding coatings exhibited excellent corrosion resistance, both of the appearance rating and protection rating reached 10⁰.

Acknowledgments The authors thank the Physical and Chemical Testing Center at Southwest Institute of Technology and Engineering for materials characterizations.

References

1. T. Sun, H.H. Teng, X.J. Jiang et al., Flow Characteristics Analysis of TC18 Titanium Alloy during Hot Deformation Based on Phase Transformation, *J. Wuhan Univ. Technol.-Mater. Sci. Edi.*, 2023, **38**(6), p 1418-1425.
2. C.C. Liu, J. Gu, M. Song et al., Evolutions of the Microstructures and Mechanical Properties of TC18 Titanium Alloy Processed by Hot-Rolling in β Single-Phase Region, *J. Mater. Res. Technol.*, 2023, **26**, p 5337-5346.
3. F. Li, L. Wu, H. Zhao et al., Achieving Superior Mechanical Properties in Electron Beam Welded Joints of Ti-5Al-5Mo-5V-1Cr-1Fe Alloy Thick Plate Using Novel Annealing Treatments, *Mater Charact*, 2023, **195**, 112548.
4. B. He, X.J. Tian, X. Cheng et al., Effect of Weld Repair on Microstructure and Mechanical Properties of Laser Additive Manufactured Ti-55511 Alloy, *Mater. Des.*, 2017, **119**, p 437-445.
5. J. Zhang, W.N. Wu and L.Z. Zhao, Research Progress and Development Trend of Laser Cladding, *Hot Work. Technol.*, 2013, **42**(6), p 131-134, 139.
6. L. Zhu, P. Xue, Q. Lan et al., Recent Research and Development Status of Laser Cladding: A Review, *Opt. Laser Technol.*, 2021, **138**, 106915.
7. J.W. Yeh, Y.L. Chen, S.J. Lin et al., High-Entropy Alloys-A New Era of Exploitation, *Mater. Sci. Forum*, 2007, **560**, p 1-9.

8. W. Zhang, P.K. Liaw, and Y. Zhang, Science and Technology in High-Entropy Alloys, *Sci. China Mater.*, 2018, **61**(1), p 2–22.
9. Y. Shi, L. Collins, R. Feng et al., Homogenization of Al_xCoCrFeNi High-Entropy Alloys with Improved Corrosion Resistance, *Corros. Sci.*, 2018, **133**, p 120–131.
10. Q. Lu, X. Chen, W. Tian et al., Corrosion Behavior of a Non-equiatom CoCrFeNiTi High-Entropy Alloy: A Comparison with 304 Stainless Steel in Simulated Body Fluids, *J. Alloy. Compd.*, 2022, **897**, 163036.
11. K.Y. Tsai, M.H. Tsai and J.W. Yeh, Sluggish Diffusion in Co-Cr-Fe-Mn-Ni High-Entropy Alloys, *Acta Mater.*, 2013, **61**(13), p 4887–4897.
12. C.Y. Cheng, Y.C. Yang, Y.Z. Zhong et al., Physical Metallurgy of Concentrated Solid Solutions from Low-Entropy to High-Entropy Alloys, *Curr. Opin. Solid State Mater. Sci.*, 2017, **21**(6), p 299–311.
13. J. Pan, T. Dai, T. Lu et al., Microstructure and Mechanical Properties of Nb₂₅Mo₂₅Ta₂₅W₂₅ and Ti₈Nb₂₃Mo₂₃Ta₂₃W₂₃ High Entropy Alloys Prepared by Mechanical Alloying and Spark Plasma Sintering, *Mater. Sci. Eng. A*, 2018, **738**, p 362–366.
14. Z. Gu, S. Xi and C. Sun, Microstructure and Properties of Laser Cladding and CoCr_{2.5}FeNi₂Ti_x High-Entropy Alloy Composite Coatings, *J. Alloys Compd.*, 2020, **819**, p 152986.
15. C.C. Sun, Y. Zhang, J. Zhang et al., Progress in Corrosion Resistance of CoCrFeNi High Entropy Alloys, *Spec. Cast. Non-ferrous Alloys*, 2020, **40**(5), p 557–562.
16. X.Y. Wang, Q. Liu, H.T. Ren et al., Effects of Ti Content on Hardness and Wear Resistance of CoCrFeNiTi High-Entropy Alloy Coatings, *Surf. Technol.*, 2023, **52**(1), p 47–55.
17. S. Zhang, B. Han, M. Li et al., Investigation on Solid Particles Erosion Resistance of Laser Cladded CoCrFeNiTi High Entropy Alloy Coating, *Intermetallics*, 2021, **131**, 107111.
18. H. Liu, W. Gao, J. Liu et al., Microstructure and Properties of CoCrFeNiTi High-Entropy Alloy Coating Fabricated by Laser Cladding, *J. Mater. Eng. Perform.*, 2020, **29**, p 7170–7178.
19. R.Y. Zuo, R.L. Sun, W. Niu et al., Microstructure and Properties of CoCrFeNiTi_x High Entropy Alloy Coated by Laser Cladding, *Surf. Technol.*, 2022, **51**(3), p 363–370.
20. K. Slipchenko, B. Volodymyr, S. Denys et al., Multicomponent Binders for PcBN Performance Enhancement in Cutting Tool Applications, *J. Eur. Ceram. Soc.*, 2022, **42**(11), p 4513–4527.
21. C. Ding, X. Cui, J. Jiao et al., Effects of Substrate Preheating Temperatures on the Microstructure, Properties, and Residual Stress of 12CrNi2 Prepared by Laser Cladding Deposition Technique, *Materials*, 2018, **11**(12), p 2401.
22. H.Z. Wang, Y.H. Cheng, J.Y. Yang et al., Microstructure and Properties of Fe Based Amorphous Coatings Deposited by Laser Cladding under Different Preheating Temperatures, *J. Non-Cryst. Solids*, 2023, **602**, 122081.
23. Z.X. Zhu, X.B. Liu, Y.F. Liu et al., Microstructure and High Temperature Tribological Properties of Laser Cladding FeCoCrNi-Based High-Entropy Alloy Coatings, *J. Mater. Eng.*, 2023, **51**(3), p 78–88.
24. GJB 150.11A-2009. *Laboratory Environmental Test Methods for Military Material—Part 11: Salt fog Test [S]*, The General Reserve Department of PLA, Beijing, 2009.
25. ISO/TR 26946-2011. *Standard Method for Porosity Measurement of Thermally Sprayed Coatings [S]*, International Organization and Standardization, Switzerland, 2011.
26. Hu J. *Experimental Study on of Laser Cladding Ti_{0.8}CoCrFeNi High-Entropy Alloy Composite Coating on TC21 Titanium Alloy [D]*, Dalian University of Technology, Dalian, 2021.
27. T. Yu, *Wear Resistant Composite Coatings Prepared by Laser Cladding on Ti-6Al-4V*, Shandong University, Jinan, 2018.
28. X. Qiao, T. Xia and P. Chen, Numerical Research on Effect of Overlap Ratio on Thermal-Stress Behaviors of the High-Speed Laser Cladding Coating, *Chin. Phys. B*, 2021, **30**(1), 018104.
29. F. Fu, Y. Zhang, G. Chang et al., Analysis on the Physical Mechanism of Laser Cladding Crack and Its Influence Factors, *Optik*, 2016, **127**(1), p 200–202.
30. A. Takeuchi and A. Inoue, Classification of Bulk Metallic Glasses by Atomic Size Difference, Heat of Mixing and Period of Constituent Elements and Its Application to Characterization of the Main Alloying Element, *Mater. Trans.*, 2005, **46**(12), p 2817–2829.
31. J. Hu, X.M. Sui, L. Zhang et al., Effects of TiN Content on Microstructures and Properties of Ti_{0.8}CoCrFeNiAl_{0.5} High-Entropy Alloy Composite Coating, *Aeronaut. Manuf. Technol.*, 2021, **64**(19), p 71–79.
32. Y. Fang, X.H. Jia, J.B. Lei et al., Wear Resistance and Electrochemical Corrosion Properties of 60 wt% Coarse and Fine WC Composite NiCu Alloy by Laser Melting Deposition, *Acta Mater. Compos. Sin.*, 2022, **39**(7), p 3498–3509. ((in Chinese))
33. V.V. Dushik, G.V. Redkina, N.V. Rozhanskii et al., Corrosion and Electrochemical Behavior of β-W CVD Coatings in NaCl Solution, *Prot. Met. Phys. Chem. Surf.*, 2020, **56**(7), p 1321–1324.
34. W.K. Yu, *Study on Preparation and Properties of Laser Cladding CoCrFeNi-X High Entropy Alloy Coatings [D]*. Huazhong University of Science & Technology (2021).
35. GB/T 6461-2002. *Methods for Corrosion Testing of Metallic and Other Inorganic Coatings on Metallic Substrates—Rating of Test Specimens and Manufactured Articles Subjected to Corrosion Tests [S]*. Beijing: General Administration of Quality Supervision, Inspection and Quarantine of the People’s Republic of China (2002).

Publisher’s Note Springer Nature remains neutral with regard to jurisdictional claims in published maps and institutional affiliations.

Springer Nature or its licensor (e.g. a society or other partner) holds exclusive rights to this article under a publishing agreement with the author(s) or other rightsholder(s); author self-archiving of the accepted manuscript version of this article is solely governed by the terms of such publishing agreement and applicable law.